

Am Chem Soc. Author manuscript; available in PMC 2011 June 30.

Published in final edited form as:

J Am Chem Soc. 2010 June 30; 132(25): 8645–8656. doi:10.1021/ja1004619.

Experimental and Theoretical EPR Study of Jahn-Teller Active [HIPTN₃N]MoL Complexes ($L = N_2$, CO, NH₃)

Rebecca L. McNaughton[‡], Michael Roemelt[§], Jia Min Chin[†], Richard R. Schrock^{†,*}, Frank Neese^{§,*}, and Brian M. Hoffman^{‡,*}

[‡]Department of Chemistry, Northwestern University, Evanston, Illinois 60208

§Institut für Physikalische and Theoretische Chemie, Universität Bonn, Wegelerstrasse 12, 53115 Bonn, Germany

[†]Department of Chemistry, Massachusetts Institute of Technology, Cambridge, Massachusetts, 02139

Abstract

The trigonally symmetric Mo(III) coordination compounds [HIPTN₃N]MoL (L = N₂, CO, NH₃; [HIPTN₃N]Mo = [(3,5-(2,4,6-i-Pr₃C₆H₂)₂C₆H₃NCH₂CH₂)₃N]Mo) are low-spin d³, S = 1/2) species that exhibit a doubly-degenerate 2E ground state susceptible to a Jahn-Teller (JT) distortion. The EPR spectra of all three complexes and their temperature and solvent dependences are interpreted within a formal '2-orbital' model that reflects the ground-state configuration, describes the vibronic interactions that lead to the JT distortions, and addresses whether these complexes exhibit static or dynamic JT distortions. The electronic and vibronic properties of these complexes are then analyzed through *ab initio* quantum chemical computations. It is not possible to interpret the spectroscopic properties of the orbitally degenerate [Mo]L with DFT methods, so we have resorted to multireference wavefunction approaches, the entry level of which is the complete active space self-consistent field (CASSCF) method. Overall the experimental and computational studies provide new insights into the role of trigonal coordination, as enforced by the [HIPTN₃N]³⁻ ligand, in activating the Mo ion for the binding and reduction of N₂.

Introduction

The coordination compound $[\mathbf{Mo}]N_2$ ($[\mathbf{Mo}] = [(3,5-(2,4,6-i-Pr_3C_6H_2)_2C_6H_3NCH_2CH_2)_3N]Mo)$, shown in Chart 1, is a crucial intermediate in the catalytic reduction of N_2 to NH_3 by protons and electrons at room temperature. 1^-6 The ability of the molybdenum center of $[\mathbf{Mo}]$ to catalytically reduce N_2 provides support for the view that the biological fixation of N_2 by the FeMo enzyme nitrogenase can take place at a single Mo center. 7^-10 Of particular importance for the study of the mechanism of dinitrogen reduction of N_2 by $[\mathbf{Mo}]$ complexes is the fact that eight of the proposed intermediates in the proposed catalytic cycle have been isolated and characterized. Central among these are the initial paramagnetic $[\mathbf{Mo}]N_2$ complex (Chart 1) and paramagnetic $[\mathbf{Mo}]NH_3$, the final state before displacement of the second NH_3 to reform $[\mathbf{Mo}]N_2$.

The $[HIPTN_3N]^{3-}$ ligand enforces a trigonal geometry on the [Mo]L complexes. This geometry confers unique electronic properties to the Mo(III) ion. In particular, [Mo]L

bmh@northwestern.edu.

complexes are uniformly low-spin (ls) d^3 species ($S = \frac{1}{2}$), one of the rarest configurations in inorganic chemistry. To our knowledge, prior to the synthesis of [\mathbf{Mo}]L there had been only one report of a ls [d^3] coordination complex,11 and few reports of organometallic ls d^3 complexes.12 A ls d^3 ion in the trigonal-bipyramidal coordination environment of [\mathbf{Mo}]L exhibits a doubly-degenerate 2E ground state (Scheme 1) that is subject to a Jahn-Teller (JT) distortion as a consequence of vibronic coupling to doubly-degenerate e vibrations.13·14 As shown in the scheme, trigonal low spin d^3 complexes have two possible electronic configurations, [$2e^3$] and [$3a^22e^1$], each doubly degenerate. Preliminary EPR studies demonstrated that the frontier orbitals of [\mathbf{Mo}]N₂ are the triply-occupied d- π doublet and gave initial insights into the vibronic properties of this complex.15

In the present study we explore the electronic and vibronic properties of $[\mathbf{Mo}]N_2$ through EPR study and formal theoretical analysis of the JT effects they disclose. In conjunction, we examine the isoelectronic $[\mathbf{Mo}]$ CO complex, which can be considered to be a model for CO-inhibited state(s) of FeMo-co, finding a remarkable equivalence in the electronic properties of the $L=N_2$ and CO complexes that can be understood through considerations of JT effects. Parallel study of the $[\mathbf{Mo}]$ NH $_3$ complex sought to address the step in catalytic N_2 reduction in which the ammonia complex, the end state of one catalytic cycle, is converted into the dinitrogen complex, the beginning state of the next. Measurements of the responses of the EPR spectra of $[\mathbf{Mo}]$ L to variations in solvent and temperature address the question of whether these complexes exhibit static or dynamic JT distortions.

The EPR spectra of all three complexes and their temperature and solvent dependences are interpreted within a formal '2-orbital' model that reflects the ground-state configuration, and describes the vibronic interactions that lead to the JT distortions. The electronic and vibronic properties of these complexes are then analyzed with ab initio quantum chemical computations, which give deep insights into the electronic structure of the [Mo]L and provide molecular interpretations of the parameters derived in the formal treatment. It should be emphasized that it is not possible to interpret the spectroscopic properties of the [Mo]L with DFT methods, 16 although they have previously given useful insights into the energetics of the catalytic cycle.17⁻19 The heart of the problem is the orbital degeneracy in the ²E ground state, which lead to very strong in-state spin-orbit coupling (SOC). This strong SOC cannot be treated by the usual linear-response approaches and the four low-lying magnetic sublevels formed by the two Kramers doublets that arise from the ²E cannot be correctly represented by two-component DFT methods. The main reason that DFT fails in this case is that it employs a single-determinant wavefunction, which does not properly account for the genuinely multi-determinantal character of the electronic ground state. Hence, the best choice is to resort to multireference wavefunction approaches, the entry level of which is the complete active space self-consistent field (CASSCF) method. Although laborious for larger molecules, this method allows one to investigate the magnetic properties of the systems along the entire JT surface(s) and to treat SOC at the same time. The missing dynamic-correlation contributions to the energetics and magnetic properties can then be approximately recovered by methods like difference-dedicated configuration interaction (DDCI20[,]21) or the related spectroscopy-oriented CI(SORCI) approach.22 This theoretical approach represents the current state-of-the-art in quantum chemical modeling of nearly orbitally degenerate transition metal complexes.

Overall the combination of experimental and computational studies gives new insights into the role of trigonal coordination, as enforced by the $[HIPTN_3N]^{3-}$ ligand, in activating the Mo ion for the binding and reduction of N_2 .

Materials & Methods

[Mo]N $_2$,23 [Mo]NH $_3$ ·23 and [Mo]CO24 were synthesized as described in the literature. All [Mo]NH $_3$ samples for EPR measurements were prepared under an Ar atmosphere with N $_2$ -free solvents (freeze-pump-thaw degassed 3 times) in order to avoid dinitrogen exchange. EPR samples were prepared under an inert atmosphere by filling EPR sample tubes with 10mM solutions of the compound desired. The tubes were subsequently sealed with grease and immediately frozen at -196° C to minimize degradation upon exposure to air. In several cases the quartz tubes were fitted with graded seals to Pyrex and the tubes were flamesealed. Samples that were flame-sealed were not kept frozen.

X-band EPR spectra were collected with a Bruker ESP300 spectrometer equipped with an Oxford ITC503 cryostat. The Simfonia program (Bruker) was used to simulate the EPR spectra.

Calculations

All calculations on the [Mo]L performed in this work were conducted with the ORCA25 quantum chemistry program package. Three different models were studied within this work. First, the untruncated complex (1); second, a truncated model where the large HIPT groups of the [Mo]L complexes were replaced by hydrogen atoms (1'); third, a model with the HIPT groups replaced by ethyl groups (1''):

Model (1) can only be treated at the DFT level and serves as a reference for the truncated models that were studied with wavefunction-based *ab initio* methods. Model 1' served as a basis for the understanding of the electronic structure of the complexes and the influence of vibronic coupling on the calculated g-tensors. Model 1' was used to more realistically model g-tensors and vibronic coupling constants.

The geometries of the [Mo]L in model 1' were optimized using a CASSCF(3,2) wavefunction together with a scalar relativistic zero'th-order regular approximation treatment (ZORA26·27) using the model potential idea of Van Wüllen28 and the appropriate scalar relativistically recontracted all-electron TZVP basis set (SARC-TZVP) described recently.29⁻³¹ Property and final energy calculations were performed with the ORCA implementation22 of the MR-DDCI2 method20·21 together with the TZVP basis set. The calculations are based on state-averaged CASSCF(3,5) reference states and orbitals as explained in detail in the main body of the paper.

Geometries of 1'' were fully optimized using the BP8632·33 functional, in conjunction with ZORA, and the SARC-TZVP basis set for molybdenum and nitrogen, and the SARC-SV(P) basis set for carbon and hydrogen.34 Spin unrestricted Kohn-Sham determinants have been chosen to describe the open shell wavefunctions. As described above, property and final energy calculations were performed with the ORCA implementation of the MR-DDCI2 method using state averaged CASSCF(3,5) reference wavefunctions.

Molecular g-tensors were calculated using the Gerloch-McMeeking35 formalism as implemented in the ORCA-MRCI program. Similar procedures have been proposed by Bolvin36 and Pierloot.37 The approach is an infinite order solution (quasi-degenerate perturbation theory, QDPT38·39) with respect to the SOC in a finite number of scalar-relativistic MR-DDCI2 (or SA-CASSCF) eigenstates.40 First order perturbation theory with the Zeeman operator is used on top of the relativistic solutions in order to determine the

effective g-values. More precisely, we start with the solutions of the previously conducted non-relativistic calculations in which the Born-Oppenheimer Hamiltonian is diagonal. Within this basis we diagonalize the spin-orbit mean-field Hamiltonian, which is an effective one-electron operator:

$$\widehat{H}_{SOMF} = \sum_{i} \widehat{h}^{SOC}(i)\widehat{s}(i) \tag{1}$$

This procedure yields pairs of Kramer's doublets ϕ and $\overline{\phi}$. If an external magnetic field is applied, these Kramer's doublets are split by the Zeeman term that is added to the Hamiltonian.

$$\widehat{H} = \widehat{H}_{BO} + \widehat{H}_{SOMF} + \widehat{H}_{Zee} \tag{2}$$

With

$$\widehat{H}_{Zee} = \mu_B(\widehat{L} + g_e \widehat{S}) B \tag{3}$$

Where μ_B is the Bohr magneton, g_e the electron Landè factor, B the magnetic flux density and \hat{L} and \hat{S} are the orbital and spin angular momentum operators, respectively. It can be shown 36 that finding the eigenvalues of the Zeeman operator in the basis of the Kramer's doublet is equivalent to finding the eigenvalues of the Zeeman term of the Spin-Hamiltonian in the basis of pseudo-spin functions $|+\rangle$ and $|-\rangle$. Eventually the g-tensors are evaluated using

$$\Gamma_{\mu\nu} = (gg^T)_{\mu\nu} = 2\sum_{I,J=\phi,\overline{\phi}} \left\langle I \left| \mathbf{L}_{\mu} + g_e \mathbf{S}_{\mu} \right| J \right\rangle \left\langle J \left| \mathbf{L}_{\nu} + g_e \mathbf{S}_{\nu} \right| I \right\rangle \tag{4}$$

Picture change effects, that arise from a mismatch of the quasirelativistic wavefunction and the non-relativistic formulation of the SOC operator,41⁻43 have been neglected for the calculation of SOC integrals since their inclusion had very little influence on the predicted g-tensors.

RESULTS

Magnetic Properties of [Mo]L; L = N₂/CO, NH₃

The X-band CW EPR spectra of the [Mo]L, L = N₂, CO and NH₃, exhibit axial symmetry (Fig. 1A) with g-values greatly shifted from the free-electron value, g = 2. Identical g-values were obtained from Q-band CW and spin-echo EPR spectra. Remarkably, the spectrum of [Mo]CO is indistinguishable from that of [Mo]N₂, with simulations of the spectra for both complexes giving $g_{\perp} = 1.51 < 2 < g_{\parallel} = 3.03.44$ The spectrum for [Mo]NH₃ differs only slightly, showing larger g shifts: $g_{\perp} = 1.35 < 2 < g_{\parallel} = 3.20$.

The g_{\parallel} feature of the $L=N_2$, CO spectra shows a low-field shoulder caused by hyperfine couplings to the 95,97 Mo (total abundance, 23%) and corresponds to $A_{\parallel} \sim 46$ G (at g=3.03) = 196 MHz. The effects of variations in temperature and solvent on these spectra are discussed below.

Simulations of these field-swept spectra require a greater linewidth for the perpendicular region than the parallel, $\sigma^B_{\perp} \approx 400~\text{G}$, $\sigma^B_{\parallel} = 180~\text{G}$. This might be taken to suggest an unresolved rhombicity in the g values, but this is not the case. The 'proper' way to analyze EPR linewidths is in the context of a presentation of intensity vs. frequency,45 which corresponds to a display on a g-value scale (Fig. 1B). Correspondingly, the linewidths on such a scale $[\sigma^{\upsilon}_{\perp}, \sigma^{\upsilon}_{\parallel}]$ are related to those on a field scale by the g-values, with $\sigma^{\upsilon}_{\perp}/\sigma^{\upsilon}_{\parallel} = g_{\perp}\sigma^B_{\perp}/g_{\parallel}\sigma^B_{\parallel}$. The result is $\sigma^{\upsilon}_{\perp}/\sigma^{\upsilon}_{\parallel} \sim 1$, and thus the spectra and simulations give no indication that the g-tensor has any rhombic character; the maximum rhombicity that could be accommodated without introducing resolved structure in the g_{\perp} region is $\delta g_{\perp} = (g_2 - g_3) \leq 0.1$.

Ligand-Field Analysis of Ground-state Configuration and g-Values

The unusual low-spin properties of these [Mo]L complexes can be attributed to the C_{3V} -symmetric coordination environment of the Mo(III) ion, which splits the five d-orbitals into two degenerate (2e) pairs and a non-degenerate (a_1) orbital (Scheme 1), where the orbitals can be expressed either as the conventional, real d-orbitals or as eigenfunctions of the z-component of the total orbital angular momentum, $m_l = 0, \pm 1, \pm 2$ (L = 2),

$$2e = \begin{bmatrix} d_{xz}, d_{yz} \end{bmatrix} = \begin{bmatrix} |1\rangle, |-1\rangle \\ 3e = \begin{bmatrix} d_{x^2-y^2}, d_{yz} \end{bmatrix} = \begin{bmatrix} |2\rangle, |-2\rangle \end{bmatrix}$$

$$3a_1 = \begin{bmatrix} d_{z^2} \end{bmatrix} = \begin{bmatrix} |0\rangle \end{bmatrix}$$
(5)

with ligand-field energies E(3e) > E(2e). Hence, three frontier orbital schemes for the central Mo(III) ion are possible.

In the two cases where $E(3a_1) > E(2e)$, the Mo(III) ion would have a ls $[2e^3]$ configuration, whereas if the inequality were reversed, the ion would have a ls $[3a_1^22e^1]$ configuration (Scheme 1). In each case the ligand-field ground state is orbitally doubly degenerate with an additional two-fold spin degeneracy. As a result, the ion exhibits a doubly-degenerate 2E ground state that is subject to a JT distortion by vibronic coupling to doubly-degenerate e vibrations.13·14

The symmetry-lowering JT interaction can be described in terms of vibronic coupling to a single composite ('interaction') e mode with force constant K. The simplest treatment incorporates only linear vibronic coupling, in which a distortion, ρ , along the interaction coordinate mixes the 2e orbitals and contributes an energy lowering,

$$H_{IT} \propto -F\rho$$
 (6)

where F is the linear JT coupling coefficient. In the familiar JT-active systems, such as octahedral Cu(II), the JT effect generates a distortion along a degenerate interaction mode, ρ_0^0 , that stabilizes the complex by an energy, E_{JT}^0 :

$$\rho_0^0 = \frac{F}{K} \\
E_{,T}^0 = \frac{F^2}{2K}$$
(7)

However, both ls d³ configurations of a trigonally symmetric [**Mo**]L exhibit unquenched orbital angular momentum and their orbital degeneracy is split by spin-orbit coupling (SOC), which competes with the JT effect. As a result of this competition the molecule

undergoes a diminished, 'pseudo Jahn-Teller' (PJT) distortion along the interaction mode coordinate of magnitude ρ_0 :13

$$\rho_0 = \sqrt{\left(\frac{F}{K}\right)^2 - \left(\frac{\lambda}{2F}\right)^2}
= \rho_0^0 \sqrt{1 - \frac{\lambda^2}{\left(4E_{JT}^0\right)^2}}$$
(8)

If the JT vibronic coupling is weak and the JT stabilization energy is small, $E_{JT}^{\ 0} < \lambda 4$, the PJT distortion is quenched and the complex retains trigonal symmetry. In contrast, when $\rho_0 > 0$, as in the normal JT effect the PJT effect replaces the 2E electronic degeneracy with a vibronic degeneracy in which the complex is distorted (e.g.: equilateral \leftrightarrow isosceles triangle of in-plane N atoms; axial \leftrightarrow non-axial N_2) and the distortion pseudo-rotates, with the phase angle defining the direction of the distortion.

One must further allow for a solvent-dependent environmental contribution to the e-orbital splitting, denoted the 'solvent potential', V_L .46 As the result of these interactions, the ground (W_-) and excited (W_+) molecular adiabatic potential energy surfaces (APES) are a function of the PJT distortion (ρ) , the phase angle (ϕ) , and V_L according to:

$$W_{\pm} = \frac{K\rho^2}{2} \pm 2\sqrt{\left(\frac{\lambda}{2}\right)^2 + (F\rho\sin(\varphi))^2 + (F\rho\cos(\varphi) + V_L)^2}$$
(9)

When $V_L=0$, the ground APES (W_) is independent of the phase angle ϕ , with the minimum of the 'trough' at ρ_0 ; this shape is well-known as the 'modified Mexican hat', Fig. 2A.13'14 When $V_L\neq 0$, the PJT distortion (ρ_0 ' eq (8)) is not altered, but the ground APES becomes 'skewed' towards the distortion direction favored by this potential, Fig. 2B. At low temperatures, the dynamic (pseudo-rotating) PJT distortion will localize at the skewed APES minimum. If quadratic JT coupling is significant, in addition to the linear term (eq (6)), this also tends to localize the distortion. It 'warps' the APES trough, generating three minima equispaced in ϕ ; these minima might correspond, for example, to the three isosceles triangles formed by appropriate displacements of the in-plane N atoms.13

To interpret the g-values and characterize the electronic structure of these [Mo]L complexes, we computed the wavefunctions for the two electronic configurations as a function of the vibronic, SOC, and solvent parameters within a 2-orbital model that treats only the partially occupied $d-\pi$ orbitals (Supporting Information): the $[3a_1^22e^1]$ configuration is treated as a single electron in the (2e) doublet whereas the $[2e^3]$ configuration is treated as a single hole in the (2e) doublet. In both cases the ground-state electronic energies and wavefunctions at the equilibrium value of the distortion are determined by r, the ratio of the sum of equilibrium distortion energy plus environmental energy (which is the off-diagonal element of the Hamiltonian matrix), to the SOC parameter. These energies are conveniently parameterized in terms of a fictitious angle, 2θ , which is defined by the dimensionless ratio, r (ref 15 and SI),

$$\tan(2\theta) \equiv r \equiv 2\frac{F\rho_0 + \frac{V_L}{2}}{\lambda} \tag{10}$$

The g-values calculated from the wavefunctions for the two electronic configurations can be written in terms of 2θ ,

$$[e_1^3]g_{\parallel} = 2(1+k\cos(2\theta)) \tag{11a}$$

$$[a^{2}e_{1}^{3}]g_{\parallel}=2(1+k\cos(2\theta)) \tag{11b}$$

$$g_{\perp} = 2\sin(2\theta) \tag{11e}$$

with the parameter k defined such that (1-k) represents the fraction of d-electron density delocalized onto the ligands; $(1-k) \to 0$ in the absence of covalency. Fig. 3 plots the g-values for the $[2e^3]$ and $[3a_1^22e^1]$ configurations as a function of r for the crystal-field limit, k = 1, and for d-electron delocalization of (1-k) = 0.22.

As r increases, 2θ increases from 0 (JT effect quenched, $\rho_0 = 0$, and no V_L ; complex 2e orbitals) to $\pi/2$ (large splitting of 2e degeneracy; real 2e orbitals), the g-values for the $[2e^3]$ configuration traverse the range, $[0 \le g_{\perp} \le 2]$ and $[4 \ge g_{\parallel} \ge 2]$, while those for $[3a_1^22e^1]$ vary as $[0 \le g_{\parallel} \le g_{\perp} \le 2]$. Introduction of covalency $(k \ne 1)$ shifts g_{\parallel} towards g = 2 in both configurations; g_{\perp} is independent of k (eq (11c)).

Examination of eqs (11a–c) and Fig. 3 reveal that the observed g-values for the [Mo]L, L = $N_2/CO/NH_3$ complexes are compatible with the [$2e^3$] configuration and eqs (11a,c) and not [$3a^22e^1$] and eqs (11b,c). Application of eqs (11a,c) reproduces the observed g-values for the L = N_2/CO complexes ($g_{\perp} = 1.51$, $g_{\parallel} = 3.03$) with a distortion/off-diagonal energy ratio, r = 1.2 and a d-electron delocalization of (1-k) = 22%. Application of these equations to [Mo]NH₃ ($g_{\perp} = 1.35$, $g_{\parallel} = 3.20$) gives r = 0.9, about three-fourths the value for the L = N_2/CO complexes, and comparable electron delocalization, (1-k) = 18%.

The PJT splitting between the ground APES minimum and the excited APES at the equilibrium value of the distortion,

$$\Delta E(\rho_0)_{PJT} = \lambda \sqrt{1 + \tan(2\theta)^2}$$
(12)

is large because SOC for Mo(III) is large, $\lambda = 800 \text{cm}^{-1}$; the values of r, k, for the $L = N_2/\text{CO}$ complexes correspond to $\Delta E_{PJT}(\rho_0) \approx 3\lambda/2 \approx 1200 \text{ cm}^{-1}$. As a result, the ground and 'coupling' or adiabatic limit), and therefore, the system and its g-values are well-described by the ground APES.13·14 The corresponding value for $L = NH_3$ is only slightly less, $\Delta E(\rho_0) \approx 1.3\lambda \sim 1000 \text{ cm}^{-1}$, and the same conclusions apply.

This analysis further allows us to understand the otherwise surprising finding that $[\mathbf{Mo}]N_2$ and $[\mathbf{Mo}]CO$ have the *same* EPR spectrum, and that the spectrum for $L = NH_3$ is so similar. In the 'normal' case of an orbitally nondegenerate $S = \frac{1}{2}$ transition ion, the g values are determined by d-orbital energy splittings, and these are established by the contributions of all ligands to the metal ion. In such a situation the ligand-field pattern for an N_2 and a CO complex would differ and so would their g-values. However, in the PJT case of $[\mathbf{Mo}]L$, for $L = N_2/CO$, the ligand field merely serves to set up an orbital configuration with an isolated orbital doublet; within that configuration the g-values are not sensitive to ligand-field parameters, but *only* to vibronic interactions (and possible solvent contributions) (eqs (11a,c)) through the ratio r (eq (10)). Given the similar structures and bonding of the two

complexes, it is understandable that the critical vibration(s) and linear vibronic coupling would be the same, and hence the g values are also the same. *Ab initio* computations presented below confirm this idea. Correspondingly, the somewhat smaller value of r for $[\mathbf{Mo}]\mathrm{NH}_3$ does not reflect differences in ligand-field parameters, but only in vibronic interactions.

Solvent Effects and JT Dynamics for [Mo]L

The g-values of $[\mathbf{Mo}]N_2$ vary with solvent (Fig. 4), $g_{\parallel} = 3.03$ (toluene); 3.10 (THF); 3.26 (octane), revealing the presence of an environmental contribution to the energetics and to the shape of the APES (V_L ; equation (9)).46 Taking the vibronic and covalency parameters in equations (10) and (11) to be independent of solvent, and viewing octane as approaching a non-perturbing environment (V_L (octane) = 0), then the g-values of $[\mathbf{Mo}]N_2$ with the other solvents provide estimates of this interaction parameters: $r_0 = 2F\rho_0/\lambda \sim 0.73$; V_L (THF)/ $\lambda \sim 0.3$; V_L (toluene)/ $\lambda \sim 0.5$. These environmental terms, with $F\rho_0 > V_L$, are small compared with those found for the PJT-active MCp_2 ·46·47 for M = Co(II), Fe(I), and Fe(III), where $F\rho_0 \ll V_L$.46·47 This relative insensitivity of $[\mathbf{Mo}]N_2$ to its environment is noteworthy, for it is in keeping with the design strategy of incorporating bulky HIPT substituents to shield the metal center from its environment. The spectra of the L = CO and NH_3 complexes in toluene and THF show even smaller changes in g-value as the solvent is varied, with only slight broadening and/or the development of shoulders observed, indicating that the complex occupies a range of solvent sites (Fig. 4).

Temperature Effects on the EPR Spectra of the [Mo]L

The g-values of [Mo]L complexes in toluene do not shift significantly with increasing temperature as illustrated for L = CO in Fig. 5, whereas in THF and octane, solvents with smaller V_L, the g-values shift only slightly. In contrast to the well-studied JT effect for octahedral Cu(II),13¹4¹48 this effective temperature invariance for [Mo]L cannot be used as evidence regarding the absence or presence of dynamic reorientation of a trapped JT distortion. JT-active Cu(II) also shows a 'Mexican hat' APES, and warping of the APES also leads to three alternate JT distortion orientations; for example, elongation of bonds along each of the three coordinate axes. Furthermore, each of the distorted Cu(II) geometries exhibits an axial g-tensor with the same g-value components as for the [Mo]L. However, for Cu(II) the g-tensor of each distorted geometry has a different orientation, with g_{||} along the distortion axis. As a result, thermally activated pseudorotation of the distortion of a Cu(II) center causes a corresponding reorientation of the g-tensor and strong 'motional' effects in the Cu(II) EPR spectrum. In contrast, g_{\parallel} for [Mo]L is oriented along the trigonal axis for all orientations (phase angles ϕ) of the PJT distortion, so reorientation can have no effect on the EPR spectrum. We instead attribute the very slight g-shifts with increasing temperature for [Mo]L to thermal excitations within the energy 'well' of the skewed APES (Fig. 2B), which is shallower for smaller values of V_L.

The g_{\perp} and g_{\parallel} features in the EPR spectra of [Mo]L in toluene also do not broaden with increasing temperature (Fig. 5), while those for the complexes in THF and octane solutions broaden only slightly. This contrasts with the extensive broadening observed in spectra of PJT-active MCp_2 complexes resulting from Orbach relaxation by low-lying states.46·47 This difference arises because the large SOC constant for Mo(III) leads to a large energy difference between the ground and excited APES (eq (12)), whereas the SOC of Co(II), for example, is much smaller and therefore so is the energy difference. This behavior of the [Mo]L complexes also indicates that they have no low-lying ligand-field excitations, in agreement with the quantum chemical computations.

Analysis of Bonding based on ab initio calculations

In order to substantiate the qualitative analysis and gain further insight into the electronic structure of the [Mo]L complexes, *ab initio* methods were applied on truncated models of the actual system; a truncated model where the HIPT groups of the [Mo]L complexes were replaced by hydrogen atoms (1') and a model where they were replaced by ethyl groups (1'') (see computational details). As discussed in the introduction, the present work deals with JT systems that are close to orbital degeneracy and hence the application of DFT is at least problematic since Kohn-Sham DFT is a single reference approach and does not apply to degenerate states. This becomes important for g-tensor calculations and for computations of the ground APES.

Geometric Structure—For the multireference *ab initio* calculations, the number of atoms is drastically reduced with truncation of the complex geometries for models 1' and 1''(Fig. 6). Therefore it is necessary to compare the calculated geometric properties of at least the first coordination shell of the Mo(III)-ion to –as far as they are available- crystallographic data6 prior to any considerations of electronic structure or g-values. This comparison already provides a first impression of the shortcomings introduced with the truncation of the complex geometries and the different quantum chemical treatment of the PJT effect (see computational details). Within model 1' the HIPT groups have been replaced by hydrogen prior to the geometry optimizations. The optimizations were then conducted with the CAS-SCF(3,2) method together with the SARC-TZVP basis set and the zero'th order regular approximation (ZORA) to take into account relativistic effects. Model 1" geometries on the other hand were obtained from a more rigorous approach. The full geometries (including the HIPT groups) were optimized using the BP86 functional in conjunction with the SARC-TZVP basis set for Molybdenum and nitrogen atoms and the SARC-SV(P) basis set for carbon and hydrogen atoms. Relativistic effects were again taken into account by the ZORA method. Subsequently the HIPT groups were replaced by ethyl groups, which in turn were optimized separately.

Table 1 summarizes the measured and calculated bond distances for the first coordination shell for [Mo]N₂ and [Mo]NH₃ for both models. All four bond distances of the Mo(III)-ion to the trisamidoamine ligand are well described by model 1'. The observed deviations between calculation and experiment are 0.03 Å or less. On the other hand model 1' significantly overestimates the bond distance to the axial N₂ and NH₃ ligand, by 0.3 Å (N₂) and 0.2 Å (NH₃). This is thought to be due to the neglect of the steric influence of the HIPT groups on the active binding site of the [Mo] complex. In the case of [Mo]N₂ underestimation of the π -backbonding from Mo(III) to N_2 (see below) by the CASSCF method weakens the Mo-N₂ bond and hence leads to an additional bond elongation. The extreme elongation of the Mo-N₂ bond within model 1' has, of course, a major effect on the electronic structure of the N_2 ligand. The competition between σ -bonding, which strengthens the N-N bond, and π -backbonding, which causes a N-N bond weakening, is substantially biased towards σ-bonding. The calculated N-N stretching frequency for model 1' displays this imbalance: A DFT calculation at the model 1' geometry of [Mo]N₂ using the BP86 functional along with the TZVP basis set and the ZORA approximation yielded a N-Nstretching frequency of 2614 cm⁻¹. Dinitrogen in the gas phase has a stretching frequency of 2331 cm⁻¹ and IR measurements of [Mo]N₂ gave a stretching frequency of 1990 cm⁻¹.23 In this computation, the strengthening of the N-N bond by σ-bonding to the Molybdenum dominates the bond-weakening effect of π -backbonding, whereas the opposite should be the case. It is noteworthy, that this imbalance is likely to be due to the underestimation of π backbonding and not an overestimation of σ -bonding. In order to at least minimize the effect of resulting errors in the subsequent electronic structure calculations, the Mo-L bond lengths of all model 1' structures have been fixed to the crystallographic value.

Model 1'' implicitly includes the steric effects of the HIPT groups, and as a result the axial bond distances significantly improve for this model. Moreover, DFT usually accounts better for π -backbonding than CASSCF. Correspondingly, the calculated N-N stretching frequency for model 1'', 2019 cm⁻¹, is close to experiment. Interestingly, the deviations of the Mo(III)- trisamidoamine bond distances from the experimental data for model 1'' are slightly less than for model 1'. Within model 1'', the predicted Mo-N bond lengths are by 5–6 pm too long, which is quite unusual for optimized structures obtained from DFT/ZORA calculations.

Electronic Structure—State averaged CASSCF(3,2) geometry optimizations with respect to the two roots defining the 2 E ground state yielded almost perfectly C_{3V} -symmetric structures. Qualitative insight into the ordering of the orbitals in this geometry was obtained from the analysis of MR-DDCI2 calculations for the ground and ligand field excited states as discussed below. The electronic structure may be most conveniently analyzed in terms of the average natural orbitals obtained from these calculations as shown in Fig. 7. The calculations provided a picture consistent with ligand field theory in which the energy of the metal d-based orbitals increases as $e(xz,yz) < e(x^2-y^2,xy) < a_1(z^2)$. The average natural orbital occupation numbers follow the same trend. In agreement with the qualitative analysis present above, the calculations predict a low-spin $[2e^3]$ configuration lowest in energy. Qualitative molecular orbital schemes for the trigonally symmetric complexes that are consistent with the MR-DDCI2 calculations are shown in Fig. 8.

In the case of [Mo]N₂ and [Mo]CO, where the central metal ion is bound to an axial π -acceptor ligand, there are three main bonding interactions. A σ -bond is formed between the d_z 2-orbital and the axial ligand- a_1 orbital. This bond is formed by a linear combination of the 2 σ -orbital of N₂ or CO and the sp3-orbital of the amine nitrogen at which the lone-pair is located. The second σ -interaction occurs between the $3e(d_x 2_{-y} 2, d_{xy})$ orbital manifold and a linear combination of atomic orbitals of the three amido ligands of the proper symmetry. In addition, there is a π -backbond involving the $2e(d_{xz}, d_{yz})$ orbitals and the π^* -orbitals of N₂ or CO. Importantly, there is no doubt from the calculations, that the a-orbital not only is much higher in energy than the triply occupied 2e-set, but is also much higher in energy than the unoccupied second e-set. This indicates that the σ -interaction between the central molybdenum and the ligands in the axial direction is stronger than the interaction with the ligands in the equatorial plane.

Low-lying Multiplets—The electronic structure description developed above is important for the ordering of the low-lying electronic configurations that in turn determine the leading SOC interactions and ultimately also the molecular g-values. Additionally, the trisamidoamine ligand might also act as a π -donor to the 2e orbitals via the equatorial binding sites. Table 2 shows the d-d transition energies for the first 2e-3e and 2e- $3a_1$ transitions for [Mo]N₂, [Mo]CO and [Mo]NH₃ obtained from MR-DDCI2 calculations.

These results nicely demonstrate the influence of π -backbonding in the N_2 and CO complexes on the d-d spectrum. The $2e{\to}3e$ doublet and quartet transition is shifted up by 2500–11500 cm⁻¹ relative to the NH₃ complex where no backbonding occurs (Fig. 8). As expected, the π -backbonding to the CO ligand is considerably stronger than that to the N_2 ligand. This is mirrored in a difference of about 2500 cm⁻¹ for the ${}^2E_a{\to}{}^2E_b(2e{\to}3e)$ and the ${}^2E_a{\to}{}^4E_a(2e{\to}3e)$ transition energies. Transitions into the $a_1(\text{Mo-d}_{z2})$ based orbital occur 4000–14,000 cm⁻¹ higher in energy. In either case is the 2E_a manifold energetically well separated from the other accessible ligand field multiplets. Importantly, the first quartet configuration (4E_a) is calculated to be considerably higher in energy than the 2E_a state. Since wavefunction based calculations tend to overstabilize such states unless a very large amount

of dynamic correlation is recovered (which requires nearly saturated basis sets that are too expensive for the present study), this is a safe conclusion.

Covalency of the axial bonds—A comparison of the calculated covalencies confirm the experimentally observed trends (Table 3). Analysis of the 2e natural orbitals from the MR-DDCI2 calculation demonstrated ~80% metal d character for [\mathbf{Mo}]N₂ but ~76% and ~93% metal d-character for [\mathbf{Mo}]CO and [\mathbf{Mo}]NH₃, respectively. These values in turn correspond to modest orbital reduction factors k of 20% (N₂), 24% (CO) and 7% (NH₃). For all three axial ligands, these values are in reasonable agreement with the heuristic values of k (see above) determined from the two-orbital ligand-field model.

These results clearly show that the axial amino ligand has very little effect on the 2e orbital set. On the other hand the numbers confirm the assumption of weak π -interactions with the equatorial ligands. It seems that the strength of these interactions is almost unaffected by the nature of the axial ligand L. But most importantly, these results underline the existence of π -backbonding from the 2e orbitals to the axial N_2 and CO ligands.

Perhaps more importantly, these results also shed insight on the effectiveness of the [Mo]L system in reducing N_2 to NH_3 . In particular, they show that π -backbonding interactions between the 2e(xz,yz) orbitals and the π^* orbitals of N_2 lead to a substantial weakening of the N-N triple bond. As a result, the N-N stretching frequency is significantly reduced to 1990 cm⁻¹, which is already well reproduced by model 1". This N-N bond activation is considered to be one of the key steps of dinitrogen reduction.

Ab initio and DFT analysis of Molecular g-values

The ligand-field type two-state model reveals the nature of the ground-state electronic configuration and describes the g-values in terms of parameters that describe the JT vibronic coupling. However, it only takes into account the 2e orbital doublet and does not explain the origin of the coupling parameters. Thus *ab initio* methods that take into account all contributions from the relevant d-d-multiplets have been applied to these questions.

The problem was approached by using 1' as the model. In order to mimic the JT distortion, the geometry of the system was reoptimized using a CASSCF(3,2) wavefunction for only one of the components of the 2 E state. As expected, this yields a distorted structure that belongs to the C_1 point group. Some insight can be obtained by constructing a linear interpolation pathway from the symmetric SA-CASSCF(3,2) geometry to the distorted CASSCF(3,2) geometry (Fig. 9). At each point of the scan the molecular g-tensor was calculated on the basis of the SA-CASSCF(3,2) wavefunctions for the JT split components of the 2 Ea ground state (2 Ea(0) and 2 Ea(1)). This amounts to an *ab initio* realization of the two-state ligand field model and computation of a slice through the APES (Eq (9), Fig. 2).

The results of the two-state SA-CASSCF(3,2) QDPT calculations follow, as expected, the results deduced from the two-state model treatment presented above. The splitting of the two lowest Kramers doublets rapidly increases with increasing geometric distortion. At the final (calculated) JT distorted geometry the splitting amount to about 600 cm⁻¹. It will be discussed below that this is probably even an underestimate because the CASSCF calculation on truncated models will give JT distortions that are too small. Hence, the considerable slope at which the two-degenerate components diverge explain why the EPR experiments only detect contributions from a single Kramers doublet – the second doublet is simply thermally inaccessible.

With increasing geometrical distortion, the calculated g-values even approach the experimental data (Table 4), although the agreement is not perfect. This is to be expected for

a number of reasons: a) the calculations that do not take into account the bulky ligands and the solvent environment are expected to underestimate the JT distortion; b) dynamic correlation is missing which will have an influence on the calculated covalencies and JT splitting and hence on the SOC; and c) the second-order SOC between the 2E_a ground state and the various excited multiplets, including the quartet states, has not been included. These subjects will be addressed in turn.

As a first step in the refinement, almost all multiplets arising from the distribution of 3 electrons in all five metal d-based orbitals were considered. Given that the ligand is made of light atoms that display very small SOC, the multiplets formed by the electrons in this manifold of metal d orbitals can be safely expected to dominate the SOC effects and hence the molecular g-values. Taking into account 30 instead of 2 roots in the QDPT calculation allows for more than 'in-state' SOC contributions to the g-tensor. The most important indirect coupling occurs for the ground state components ${}^2E_a(0)$ and ${}^2E_a(1)$ to excited 2E_h and ⁴E_a states via the x- and y-components of the SOC operator. Such coupling cannot occur in the two-state model, and their inclusion causes deviations of the g-tensor from axial symmetry at the JT distorted geometry. It must be stressed that for symmetry reasons the gtensors remain axial symmetric at the C_{3V}-symmetric structures. Numerically the excited multiplets are seen to have a significant influence on the absolute g-values ($\Delta g_{max} \sim 0.26$, Table 4) but do not change the two-state picture qualitatively. Moreover, it appears that only the g-values of [Mo]N₂ and [Mo]CO are noticeably affected by the inclusion of higher excited ligand field states. However, a closer inspection reveals that this influence is not due to the extended SOC but rather due to the influence of the extended active space with five orbitals on the PJT-splitting of the ²E ground state.

As a second step of the refinement, the influence of dynamic correlation is investigated by extending the calculations to the MR-DDCI2 level on top of a CASSCF(3,5) reference function. This is expected to result in more accurate state energies as well as more realistic covalencies and hence calculated g-values that should be closer to experiment. These expectations are indeed confirmed by the calculations. The largest impact of dynamic correlation can be observed for the $[\text{Mo}]N_2$ complex where inclusion of dynamic correlation shifts the g_3 value down by ~0.55. It is noteworthy, that the molecular g-tensor as well as the PJT splitting of $[\text{Mo}]NH_3$ is almost unaffected by inclusion of higher excited states and dynamic correlation. Table 4 contains the calculated g-values for the 2-State-CASSCF(3,2)-model and the CASSCF(3,5)-model as well as the MR-DDCI2 calculations for all three [Mo]L complexes. The calculated PJT-splittings $\Delta E_{PJT}(\rho_0)$, the energy gap between the lowest and the second lowest Kramer's doublets after diagonalizing H_{SOC} defined above in Eq 12, also are listed there.

The results of Table 4 confirm the expected dependence of the molecular g-values on changes of the vibronic coupling parameters. However, from previous studies it is known that the simple CASSCF calculations substantially underestimate the vibronic coupling,49 and indeed the values of $\Delta E_{PJT}(\rho_0)$ are noticeably less than estimated from the two-orbital model. Hence, a third step was taken to at least model the influence of the bulky HIPT substituents in a reasonable manner. Daul and co-workers50 have demonstrated the good performance of the BP functional in describing the JT distortions in transition metal complexes – it merely tends to slightly overestimate vibronic coupling, probably due to the well-known overestimation of metal-ligand covalencies (overbinding) obtained with GGA functionals. The electron donating effect of the HIPT groups on the three amido ligands can be modeled with ethyl groups that are computationally less demanding. Thus a more refined model of the complex geometry, where the HIPT groups have been replaced by ethyl groups, was optimized using a more elaborate strategy: The geometries of the untruncated complexes (including the entire HIPT groups; model 1) were optimized with the BP86

functional together with the TZVP basis set for Molybdenum and nitrogen and SV(P) for carbon and hydrogen. Analogous calculations were previously reported by Reiher and coworkers.18 Subsequently, the HIPT groups were replaced by ethyl groups in order to model the electron donating effects and reduce the computational costs for wavefunction based *abinitio* calculations to a reasonable amount. In the next step these ethyl groups were fully optimized with the same method whereas the rest of the geometries were kept fixed at the optimized geometry of 1. This defines model 1". In this way one hopes to incorporate the steric and electronic effects of the HIPT groups into the *ab initio* calculations without facing the prohibitive costs of the calculations on the full system. PJT-splittings and g-tensors have then been calculated at the MR-DDCI2 level (Table 5).

The calculated g-values now match the experimentally observed trends very well. As observed experimentally, the $[\textbf{Mo}]\text{NH}_3$ complex is predicted to have a considerably larger g_\parallel and a smaller g_\perp than $[\textbf{Mo}]\text{N}_2$ and [Mo]CO. Comparing the g-values for $[\textbf{Mo}]\text{N}_2$ and [Mo]CO, a similar relation is observed. Generally, the calculated results can be explained if one considers the order of PJT splitting, which is $\Delta E_{PJT}([\textbf{Mo}]\text{N}_2]) > \Delta E_{PJT}([\textbf{Mo}]\text{CO}]) > \Delta E_{PJT}([\textbf{Mo}]\text{NH}_3])$ and the results of the two-state model. In contrast to the results obtained for model 1', the PJT splitting of $[\textbf{Mo}]\text{N}_2$, is calculated to be slightly larger than that of [Mo]CO. Comparison of the absolute numbers to experiment shows, a that while the g-values of $[\textbf{Mo}]\text{NH}_3$ match almost perfectly, the PJT effect is overestimated for $[\textbf{Mo}]\text{N}_2$ and [Mo]CO, as manifest in the smaller values of g_\parallel relative to experiment. This underlines the difficulties to calculate the vibronic coupling with high accuracy in orbitally nearly degenerate transition metal complexes in the presence of sensitive bonding effects like π -backbonding. Nonetheless, the values of ΔE_{PJT} now more closely match those of the two-orbital model, Table 5.

Clearly, the trend of PJT splitting correlates with trends in the electronic structure of the complexes. The PJT effect is caused by an orbital degeneracy arising from an incompletely filled $2e(d_{xz},d_{yz})$ subshell. Since the coupling of the $2e(d_{xz},d_{yz})$ shell to the ligands is, among other factors, dependent on the strength of π -backbonding to the axial ligand, the PJT parameters are a function of the π -acceptor strength of CO,N₂ and NH₃. Hence it appears that the differences in the g-values can be directly correlated with the different vibronic coupling parameters. Excited states with other than the $[2e^3]$ configuration have only minor impact on the calculated spectrum because of the large energy gap between the ground state multiplet and these configurations. Nevertheless they substantially influence the JT stabilization energy via static and dynamic correlation and hence have an indirect influence on the calculated spectra.

Although all trends of the experimental data are retained in the best calculations on 1", the absolute numbers still slightly differ from the experimental data. The rhombicity in the calculated g-tensors, which arises from SOC of the ground state with excited configurations via the x- and y-components of SOC, is small enough that it would not be resolved in the experimental data (see above). The gratifyingly small remaining deviations between calculated and measured g-values may have many sources that could not be incorporated with acceptable effort (inherent errors in CASSCF and MR-DDCI2, truncation of the QDPT procedure, basis set, truncation of the model, neglect of vibrational averaging and solvent effects).

JT Coupling and Vibrational Modes—The two-state model provides the JT parameters r and k (eq (10),eqs (11)), that directly relate the g-values with the JT stabilization energy. Table 5 likewise presents the JT stabilization energy calculated as 850–1300 cm⁻¹.

The parameters of the two-orbital model depend on the force constant K, and the vibronic coupling constant F, that characterize the composite interaction mode. However, they cannot be determined individually. Instead, eq (8) can be rewritten to give F in terms of the experimentally determined r, the SOC parameter, and a value for K:

$$F = \left[\sqrt{r^2 + 1} \lambda K \right]^{1/2} \tag{13}$$

For example, taking r=1.2 ($L=N_2/CO$), $\lambda=800$ cm $^{-1}$ for Mo(III), and a force constant of K=0.15 mdyne/Å (see below), then the linear JT coupling parameter is $F=3.1\times10^3$ cm $^{-1}$ /Å. This value in turn corresponds to a PJT distortion of $\rho_0\sim0.08$ Å (eq (8)), whose small amplitude may be appreciated by comparison to the Mo-N bond length of ~2 Å.

The JT-active mode of vibration incorporated in the 2-orbital model in fact is a composite of all e modes with non-zero JT coupling, and so are the vibronic parameters in the model. To identify the JT-active modes and their relative contribution, the JT parameters for the CASSCF optimized structures were calculated (model 1'). In principle, the DFT optimized structures (model 1'') would probably have given better results, but the flexibility of the ethyl groups obscured a detailed vibronic coupling analysis. As outlined above, two sets of model 1' geometries were obtained from our previous calculations. The first set was optimized to the fully C_{3V} -symmetric limit (see above) and was therefore used as reference. Optimization procedures of the second set took PJT effects into account and therefore led to JT-distorted structure. Subtraction of the two sets of coordinates gives the geometrical distortion arising from the PJT effect in Cartesian coordinates. Projection of these difference Cartesian coordinates onto the normal modes of the system in the C_{3V} -symmetric limit reveals the JT-active vibrations.

The nuclear Hamiltonian is the starting point for this procedure. It reads,

$$\widehat{H}_{N} = \sum_{i}^{3N} \frac{p_{x,i}^{2}}{2m_{i}} + \frac{1}{2} \sum_{i}^{3N} \sum_{j}^{3N} V_{ij} x_{i} x_{j}$$
(14)

where $p_{x,i}^2$ is the momentum operator of nucleus i in the space representation, m_i the mass of

nucleus i and $V_{ij} = \frac{\partial E}{\partial x_i \partial x_j}$ the second derivative of the electronic energy with respect to nuclear displacements along $\mathbf{x_i}$ and $\mathbf{x_j}$. The matrix \mathbf{V} is the so-called molecular Hessian. Introducing mass weighted coordinates, this can be rewritten as

$$\widehat{H}_{N} = \sum_{i}^{3N} \frac{p_{xmw,i}}{2} + \frac{1}{2} \sum_{i}^{3N} \sum_{j}^{3N} U_{i,j} x_{mw,i} x_{mw,j}$$
(15)

with

$$x_{mw,i} = \sqrt{m_i} x_i$$

$$\overrightarrow{P}_{mw,i} = \frac{\overrightarrow{P}_i}{\sqrt{m_i}}$$

$$U_{ij} = \frac{V_{ij}}{\sqrt{m_i m_j}}$$
(16)

U is called the mass-weighted molecular Hessian. V and U are real and symmetric and thus can be diagonalized by unitary transformation matrices T and L:

$$\mathbf{P}_{\mathbf{X}} = \mathbf{T}^{T} \mathbf{V} \mathbf{T} \text{ and } \mathbf{W} = \mathbf{L}^{T} \mathbf{U} \mathbf{L}$$
(17)

With

$$P_{x,ij} = k_i \delta_{ij}$$
 and $W_{Q,ij} = \omega_i^2 \delta_{ij}$ (18)

Here k denotes the force constant of the respective internal mode i and ω_i the angular frequency of the respective normal mode i. Since six eigenvectors that correspond to molecular translation and rotation have vanishing eigenvalues the space spanned by these eigenvectors is projected out before the diagonalization-step. The transformation matrices T and L are now used to evaluate the projection of geometry differences onto internal or normal modes. The projection vectors Δ_i on internal modes and Δ_Q on normal modes respectively are given by

$$\Delta_i = \mathbf{T}^T \mathbf{D}
\Delta_{\mathcal{Q}} = \mathbf{L}^T \mathbf{D}^{(m)}$$
(19)

where \mathbf{D} and $\mathbf{D}^{(m)}$ are the geometry differences in Cartesian and mass-weighted Cartesian coordinates, respectively. A more detailed description of the procedure including Input files for the ORCA25 program and considerations of scans along a linear pathway between two structures is given in the Supporting Information.

Upon application of this procedure, strong state-mixing in the vicinity of the C_{3V} -symmetric structures caused an unreasonable partitioning of the numerically calculated Hessian matrix, and it was found that ten to twelve modes of vibration have non-negligible contributions to the PJT distortion. Projection of the difference Cartesian coordinates onto the internal modes of the C_{3V} -symmetric system on the other hand yielded much better results. It indicates that the geometrical distortion arising from vibronic coupling is dominated by only one pair of degenerate bending modes of the equatorial amido-ligands that have additional limited contributions from axial ligand bending motion (Fig. 10). This confirms the above suggestions as to why the PJT effect leads to the same g-values for the $L=N_2$ and CO complexes. But it has to be stressed, that the projection gave a distribution of the geometric displacement among the internal modes that had considerable contributions from at least six to ten modes, even though the two modes shown in Fig. 10 dominate the distortion.

The vibrational force constants for the pair of JT active modes were calculated to be 0.1–0.15 mDyn/Å. Due to the inherent errors of the numerically calculated Hessian matrix calculation arising from the strong state-mixing, these numbers are only crude approximations to the true force constants.

Inserting the calculated PJT-splittings ΔE_{PJT} and geometrical distortions along the PJT-active modes ρ_0 , which are calculated to be in the order of ~0.10–0.15 Å, for the three complexes into

$$F = \frac{\sqrt{\Delta E_{PJT}^2 - \lambda^2}}{2\rho_0} \tag{20}$$

and taking $\lambda=800~cm^{-1}$, leads to first order vibronic coupling parameters $F(N_2)=3.5\times10^3~cm^{-1}/\text{Å}$, $F(CO)=4.8\times10^3~cm^{-1}/\text{Å}$ and $F(NH_3)=1.1\times10^3~cm^{-1}/\text{Å}$. The computationally calculated vibronic coupling constants are in the same order of magnitude as those predicted by the ligand field type model and fit the previously observed trends. These results highlight the effect of π -backbonding on the vibronic coupling parameters. The value of F increases with the strength of π -backbonding to the axial ligand L. Since [Mo]NH₃ exhibits no π -backbonding at all, its value is much lower than for the other two complexes.

DISCUSSION

In this study we have presented EPR spectra of three Mo(III), $S = \frac{1}{2}$, complexes, [Mo]L, $L = N_2$, CO, and NH_3 . The first and third of these complexes represent the first and last steps in the catalytic cycle for N_2 reduction, whereas the CO complex represents an inhibited form. The magnetic properties of these complexes can be understood in terms of the ligand-field orbital pattern imposed on the ls Mo(III) ion by the trigonally symmetric TAA ligand. The frontier orbitals are an orbitally degenerate 2e doublet that is isolated from the other d-molecular orbitals and that undergoes a PJT distortion in the vibronic strong-coupling (adiabatic) limit.

The g-values of these complexes are successfully analyzed within a 2-state model for the JT effect of a ls Mo(III) with a $[2e^3]$ electronic configuration. The model is parametrized in terms of (i) the constant, F, representing the linear vibronic coupling between the electronic energies and the composite doubly-degenerate vibration, and (ii) the force constant for that vibration; it does not explicitly involve any ligand-field parameters. In addition, it appears that interactions with the environment and/or second-order vibronic terms localize the PJT distortion of $[Mo]N_2$ at low temperatures. These dependencies on vibronic features and independence of ligand-field effects explain the otherwise surprising observation that the EPR spectra for $L = N_2$ and CO in toluene are indistinguishable, and that the spectrum for $L = NH_3$ is only modestly different from the other two.

The two-state ligand field model further allows a clear understanding of the physics behind the very large shifts in the g-values from the free-electron value. Within this model the spin-orbit coupling affects the system only via its z-component. This coupling leads to a strong enhancement of the magnetic moment along z, and hence g_{\parallel} , because the orbital and spin angular momenta are coupled parallel to each other. At the same time the spin-orbit coupling quenches the magnetic moments along the x- and y-axes, decreasing g_{\perp} . The JT distortion acts to weaken both effects of spin-orbit coupling. As a result, both effects decrease as the coupling parameter (r) increases. This is reflected in a progressive decrease of g_{\parallel} and increase in g_{\perp} (Fig. 3).

In agreement with previous calculations 18 we calculated the ammonia-for-dinitrogen exchange to be exergonic by 23 kcal/mol, \sim 8200 cm⁻¹ (on a BP86/TZVP/ZORA level). The present results show that this energy is the same order of magnitude as the JT-stabilization energy as calculated with eq 7. Thus the stabilization energies for the JT-distorted complexes are sufficiently large that they may well have a significant influence on catalysis - on the energetics of the reduction of [Mo]N₂ and in particular on a key step in catalysis, ligand replacement resulting in the formation of [Mo]N₂ from [Mo]NH₃ at the end of one catalytic cycle and the beginning of the next.

Beyond this, our considerations make it clear that it is the C_{3V} -symmetric environment of the Mo(III) center that enables the [Mo] complex to bind and activate N_2 by setting up a dorbital pattern that allows for significant π -backbonding from the 2e(xz,yz) orbital manifold to the unoccupied π -antibonding orbitals of N_2 (and CO) (Fig. 8), while the absence of π -backbonding to NH₃ helps facilitate the NH₃/N₂ exchange that is vital for catalysis. The π -backbonding significantly contributes to the isolation of the orbitally degenerate ground-state multiplet, which in turn is responsible for the large g-shifts via vibronic spin-orbit and vibronic coupling, whose energetic consequences likely play a significant catalytic role.

Supplementary Material

Refer to Web version on PubMed Central for supplementary material.

Acknowledgments

This work has been supported by the NIH (GM 31978, RRS; HL 13531, BMH) and the NSF (MCB0723330, BMH). FN and MR gratefully acknowledge the SFB 813 ('Chemistry at Spin Centers') and the University of Bonn for financial support.

Citations

- 1. Schrock RR. Acc. Chem. Res. 2005; 38:955–962. [PubMed: 16359167]
- 2. Schrock RR. Angew. Chem. Int. Ed. 2008; 47:5512-5522.
- 3. Yandulov DV, Schrock RR. Science. 2003; 301:76–78. [PubMed: 12843387]
- Ritleng V, Yandulov DV, Weare WW, Schrock RR, Hock AS, Davis WM. J. Am. Chem. Soc. 2004; 126:6150–6163. [PubMed: 15137780]
- 5. Yandulov DV, Schrock RR. Inorg. Chem. 2005; 44:1103–1117. [PubMed: 15859292]
- 6. Yandulov DV, Schrock RR. Inorg. Chem. 2005; 44:5542.
- 7. Burgess BK, Lowe DJ. Chem. Rev. 1996; 96:2983–3011. [PubMed: 11848849]
- 8. Hardy, RWF.; Bottomley, F.; Burns, RC. Treatise on Dinitrogen Fixation. New York: Wiley-Interscience; 1979.
- 9. Veeger, C.; Newton, WE. Advances in Nitrogen Fixation Research. Boston: Dr. W. Junk/Martinus Nijhoff; 1984.
- 10. Coughlan, MP. Molybdenum and Molybdenum-containing Enzymes. New York: Pergamon; 1980.
- 11. Rossman GR, Tsay FD, Gray HB. Inorg. Chem. 1973; 12:824-829.
- Arnold J, Wilkinson G, Hussain B, Hursthouse MB. J. Chem. Soc., Chem. Commun. 1988:1349– 1350.
- 13. Bersuker, IB. The Jahn-Teller Effect. First ed. Cambridge: Cambridge University Press; 2006.
- Englman R. The Jahn-Teller Effect in Molecules and Crystals. (Monographs in Chemical Physics Series). 1972
- McNaughton RL, Chin JM, Weare WW, Schrock RR, Hoffman BM. J. Am. Chem. Soc. 2007; 129:3480–3481. [PubMed: 17341079]
- 16. Bersuker IB. J. Comput. Chem. 1997; 18:260-267.
- 17. Studt F, Tuczek F. Angew. Chem. Int. Ed. 2005; 44:5639-5642.
- 18. Le Guennic B, Kirchner B, Reiher M. Chem. Eur. J. 2005; 11:7448-7460.
- Schenk S, LeGuennic B, Kirchner B, Reiher M. Inorg. Chem. 2008; 47:3634–3650. [PubMed: 18357978]
- 20. Miralles J, Daudey J-P, Caballol R. Chem. Phys. Lett. 1992; 198:555-562.
- 21. Miralles J, Castell O, Caballol R, Malrieu J-P. Chem. Phys. 1993; 172:33-43.
- 22. Neese F. J. Chem. Phys. 2003; 119:9428-9443.
- Yandulov DV, Schrock RR, Rheingold AL, Ceccarelli C, Davis WM. Inorg. Chem. 2003; 42:796–813. [PubMed: 12562193]

24. Byrnes MJ, Dai X, Schrock RR, Hock AS, Mueller P. Organometallics. 2005; 24:4437–4450.

- 25. Neese, F. Version 2.6.35 ed. University of Bonn; 2009.
- 26. van Lenthe E, Baerends EJ, Snijders JG. J. Chem. Phys. 1993; 99:4597-4610.
- 27. Heully JL, Lindgren I, Lindroth E, Lundqvist S, Maartensson-Pendrill AM. J. Phys. B: At. Mol. Phys. 1986; 19:2799–2815.
- 28. van Wüllen C. The Journal of Chemical Physics. 1998; 109:392.
- 29. Schaefer A, Huber C, Ahlrichs R. J. Chem. Phys. 1994; 100:5829-5835.
- 30. Eichkorn K, Weigend F, Treutler O, Ahlrichs R. Theor. Chem. Acc. 1997; 97:119-124.
- 31. Pantazis DA, Chen X-Y, Landis CR, Neese F. J. Chem. Theory Comput. 2008; 4:908–919.
- 32. Becke AD. Physical Review A: Atomic, Molecular, and Optical Physics. 1988; 38:3098-3100.
- 33. Perdew JP. Phys. Rev. B. 1986; 33:8822-8824.
- 34. Schaefer A, Horn H, Ahlrichs R. J. Chem. Phys. 1992; 97:2571–2577.
- 35. Gerloch M, McMeeking RF. J. Chem. Soc., Dalton Trans. 1975:2443-2451.
- 36. Bolvin H. ChemPhysChem. 2006; 7:1575–1589. [PubMed: 16810728]
- 37. Vancoillie S, Malmqvist P, Pierloot K. ChemPhysChem. 2007; 8:1803. [PubMed: 17647251]
- 38. Ganyushin D, Neese F. J. Chem. Phys. 2006; 125 024103/024101-024103/024111.
- 39. Neese F, Petrenko T, Ganyushin D, Olbrich G. Coord. Chem. Rev. 2007; 251:288–327.
- 40. Neese F. J. Chem. Phys. 2005; 122 034107/034101-034107/034113.
- 41. Kelloe V, Sadlej AJ, Hess BA. J. Chem. Phys. 1996; 105:1995-2003.
- 42. Newton TD, Wigner EP. Reviews of Modern Physics. 1949; 21:400–406.
- 43. Baerends EJ, Schwarz WHE, Schwerdtfeger P, Snijders JG. J. Phys. B: At., Mol. Opt. Phys. 1990; 23:3225–3240.
- 44. The simulations give a slightly lower value of the perpendicular g-value than reported previously, 1.6
- 45. Pilbrow, JR. Transition Ion Electron Paramagnetic Resonance. Oxford: Clarendon Press; 1990.
- 46. Ammeter JH. J. Magn. Reson. 1978; 30:299-325.
- 47. Ammeter JH, Swalen JD. J. Chem. Phys. 1972; 57:678-698.
- 48. Hitchman MA, Yablokov YV, Petrashen VE, Augustyniak-Jablokov MA, Stratemeier H, Riley MJ, Lukaszewicz K, Tomaszewski PE, Pietraszko A. Inorg. Chem. 2002; 41:229–238. [PubMed: 11800611]
- 49. Liakos DG, Ganyushin D, Neese F. Inorg. Chem. 2009; 48:10572–10580. [PubMed: 19845329]
- 50. Bellafrouh K, Daul C, Gudel HU, Gilardoni F, Weber J. Theor. Chim. Acta. 1995; 91:215-224.

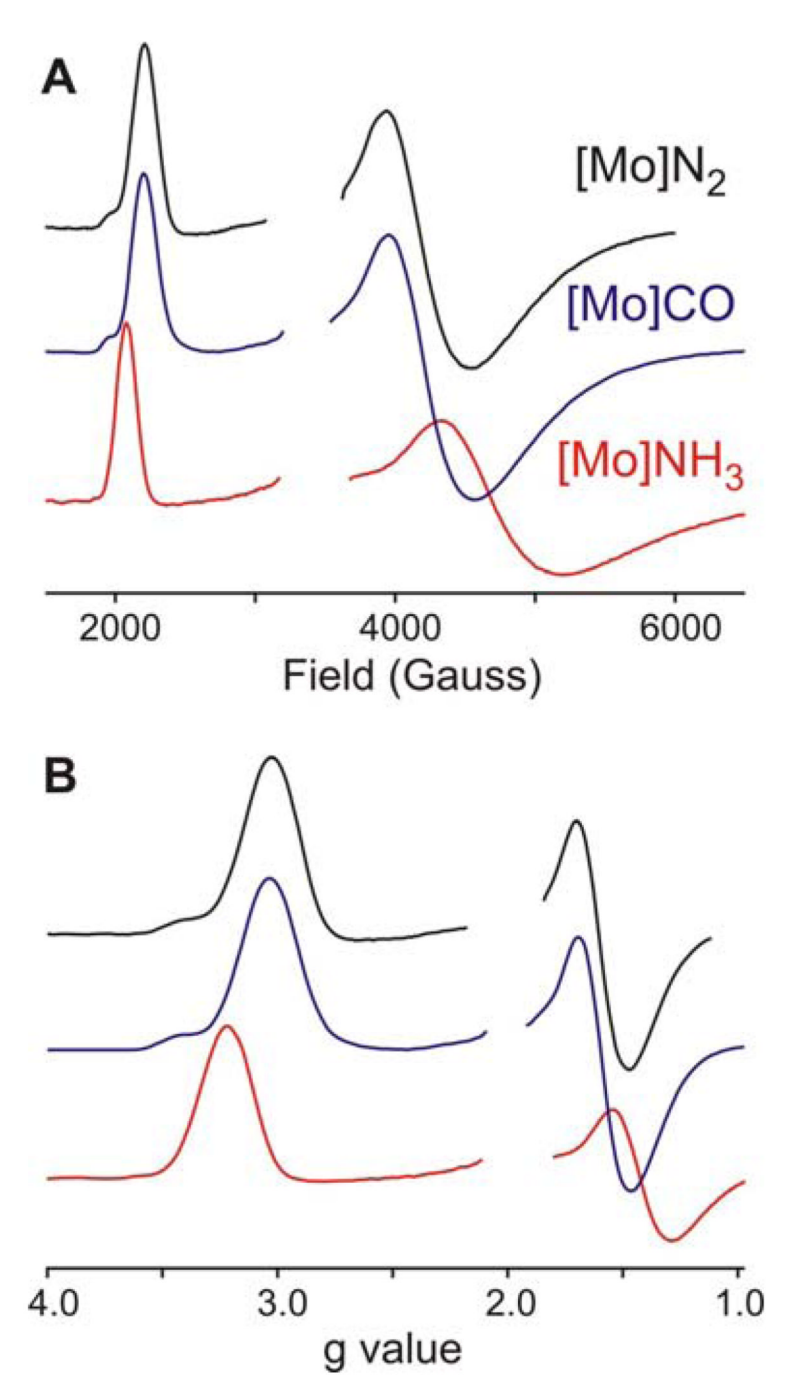


Figure 1. 10K X-band EPR spectra of $[Mo]N_2$, [Mo]CO, and $[Mo]NH_3$ in toluene, displayed in units of field (A) and g(B).

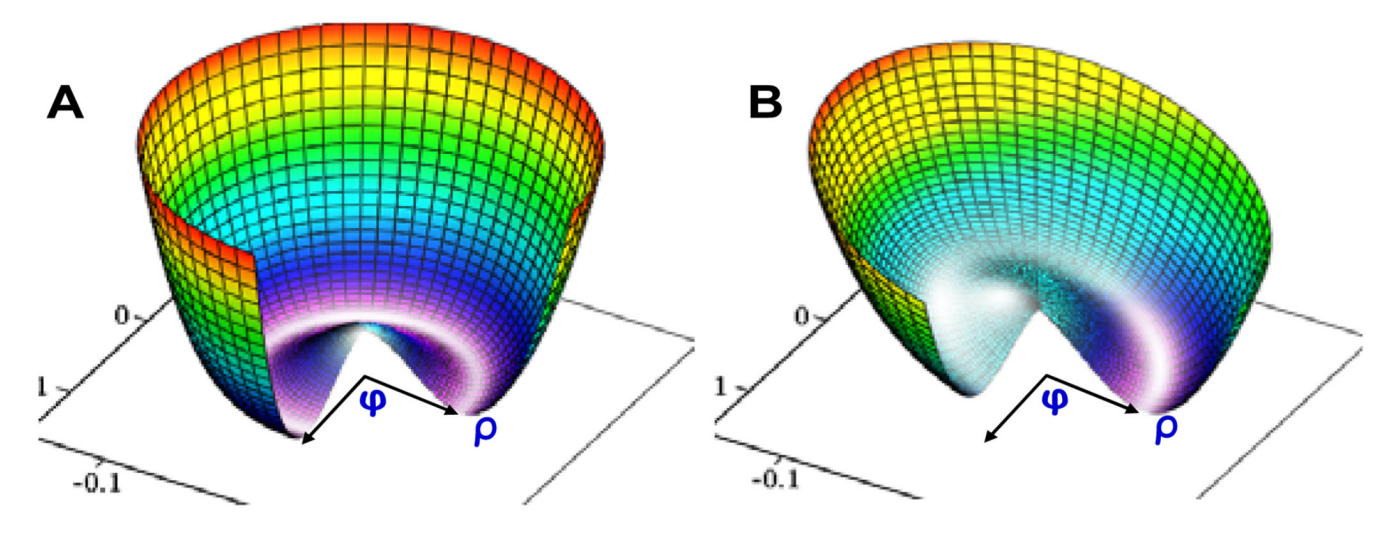


Figure 2. Lower PJT APES (W_) calculated with (A) $\lambda=800$ cm-1, K=1 mdyn/A, $F\rho_0=0.95\lambda$; (B) as in A, but with $V_L=0.1\lambda$.

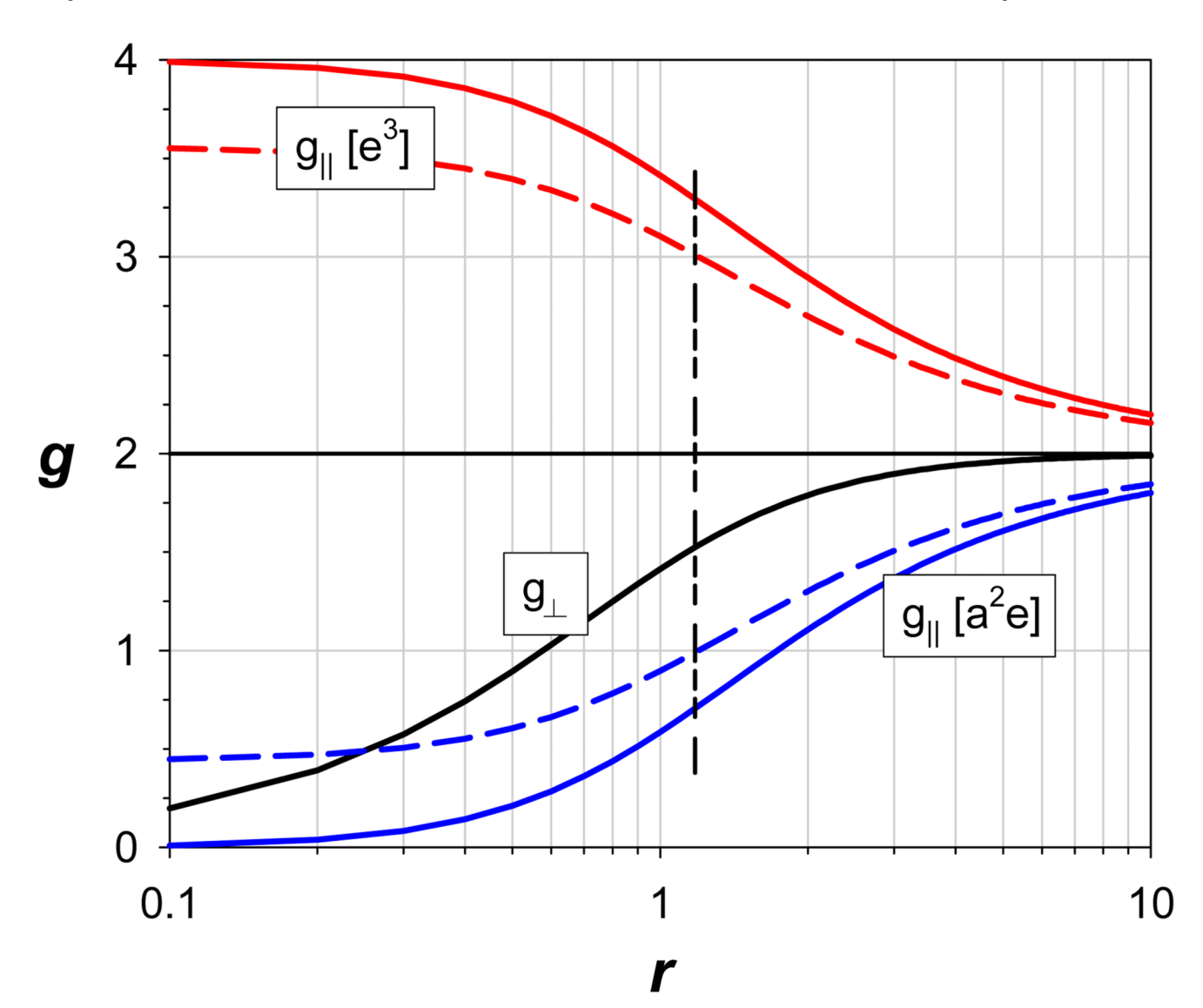


Figure 3. Plot of g-values for the $[2e^3]$ and $[3a_1^2 2e^1]$ configurations as a function of r(eq (10)). The solid red and blue lines represent the crystal field limit, k = 1; the dashed lines include delectron delocalization of (1-k) = 22%; the vertical black dashed line indicates the r value corresponding to the observed g values of $[Mo]N_2$ and [Mo]CO in toluene.

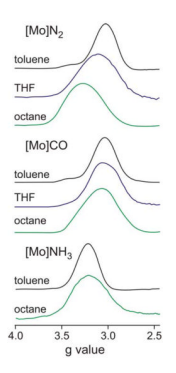


Figure 4.10K X-band EPR of [**Mo**]L complexes in toluene (black), THF (blue), and octane (green).

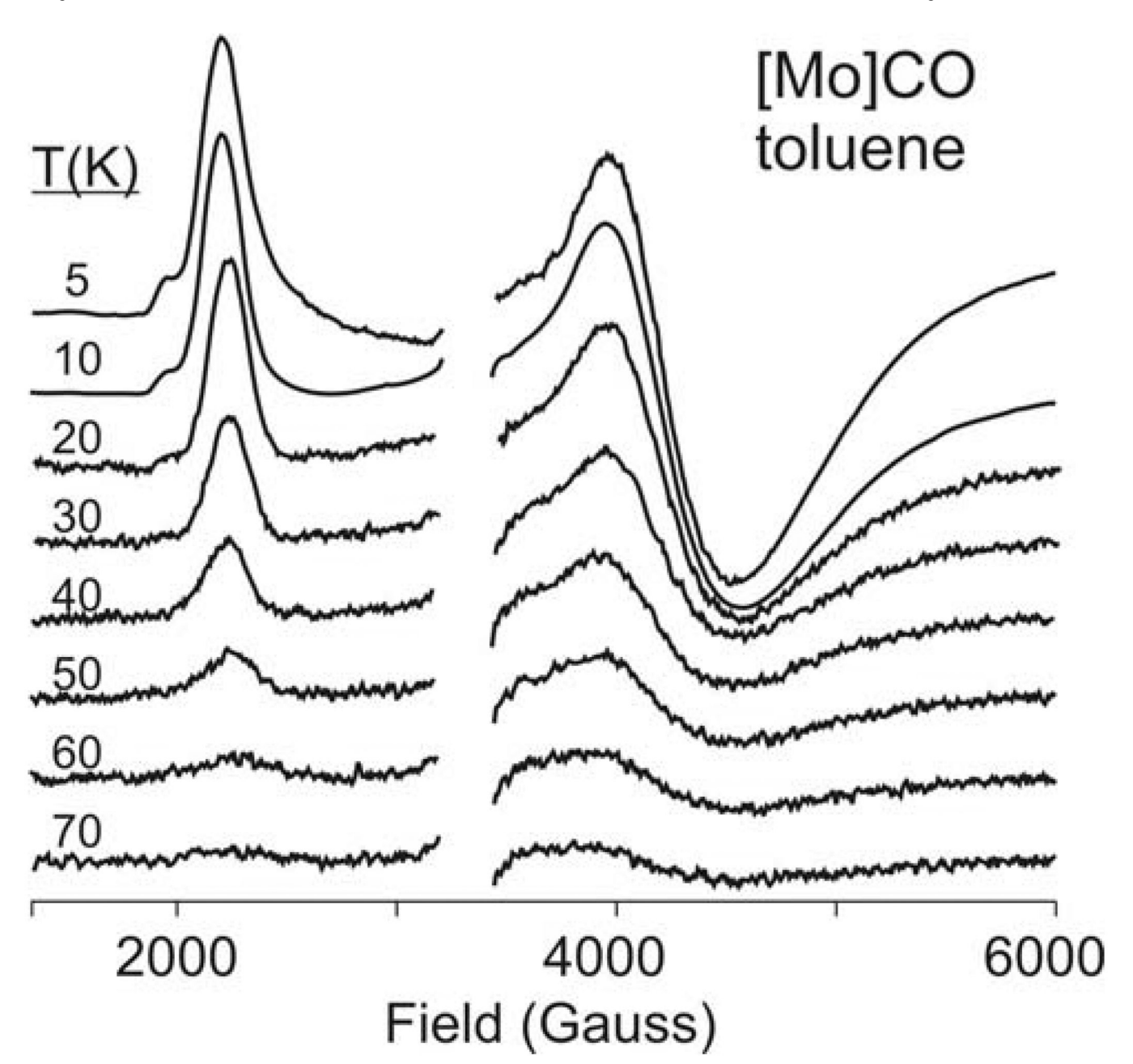


Figure 5. Variable temperature X-band EPR of [**Mo**]CO in toluene.

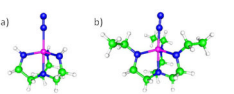


Figure 6.

Ball and Stick visualization of $[\mathbf{Mo}]N_2$ model geometries $\mathbf{1}'(a)$ and $\mathbf{1}''$ (b). The HIPT groups have been replaced by hyrdogen atoms (a) or ethyl groups (b). Model $\mathbf{1}'$ geometries were optimized on a CASSCF(3,2)/TZVP/ZORA level of theory. Model $\mathbf{1}''$ originate from optimizations of the full geometry including HIPT groups on a BP86/TZVP(Mo,N)/SV(P) (C,H)/ZORA level of theory. The subsequently introduced ethyl groups have been optimized seperately with the same method.

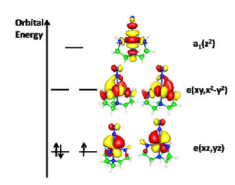


Figure 7.Qualitative molecular orbital diagram for the electronic ground state of **1**' as obtained from MR-DDCI2:CAS(3,5)/TZVP/ZORA calculations. Shown are natural orbitals.

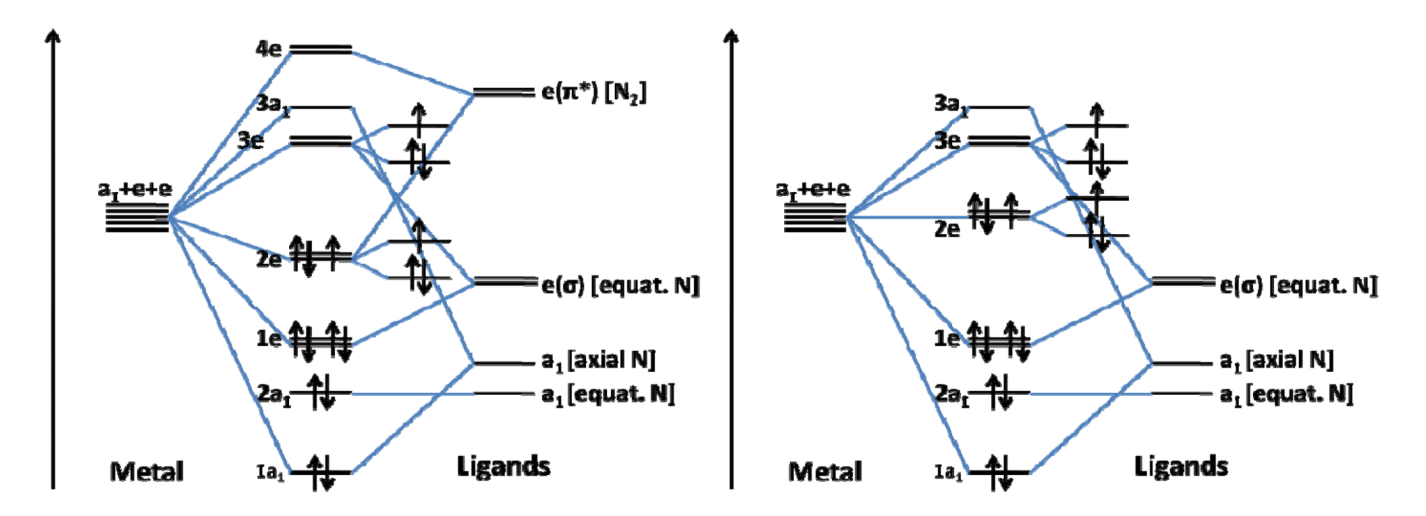


Figure 8. Qualitative molecular orbital schemes for [Mo]N₂/CO (left) and [Mo]NH₃ (right). While for [Mo]N₂ and [Mo]CO π -backbonding significantly stabilizes the 2e orbitals, there is no such stabilization in the case of [Mo]NH₃. Minor π -interactions of the equatorial ligands to the 2e orbitals are not shown.

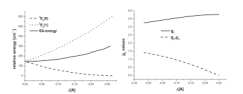


Figure 9. Calculated energies (left) and g-values (right) of the scan along a linear interpolation pathway between the symmetric and distorted structure of [Mo]NH₃. Computational Details: SA-CASSCF(3,2)/TZVP/ZORA.

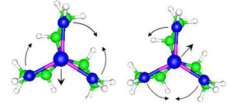
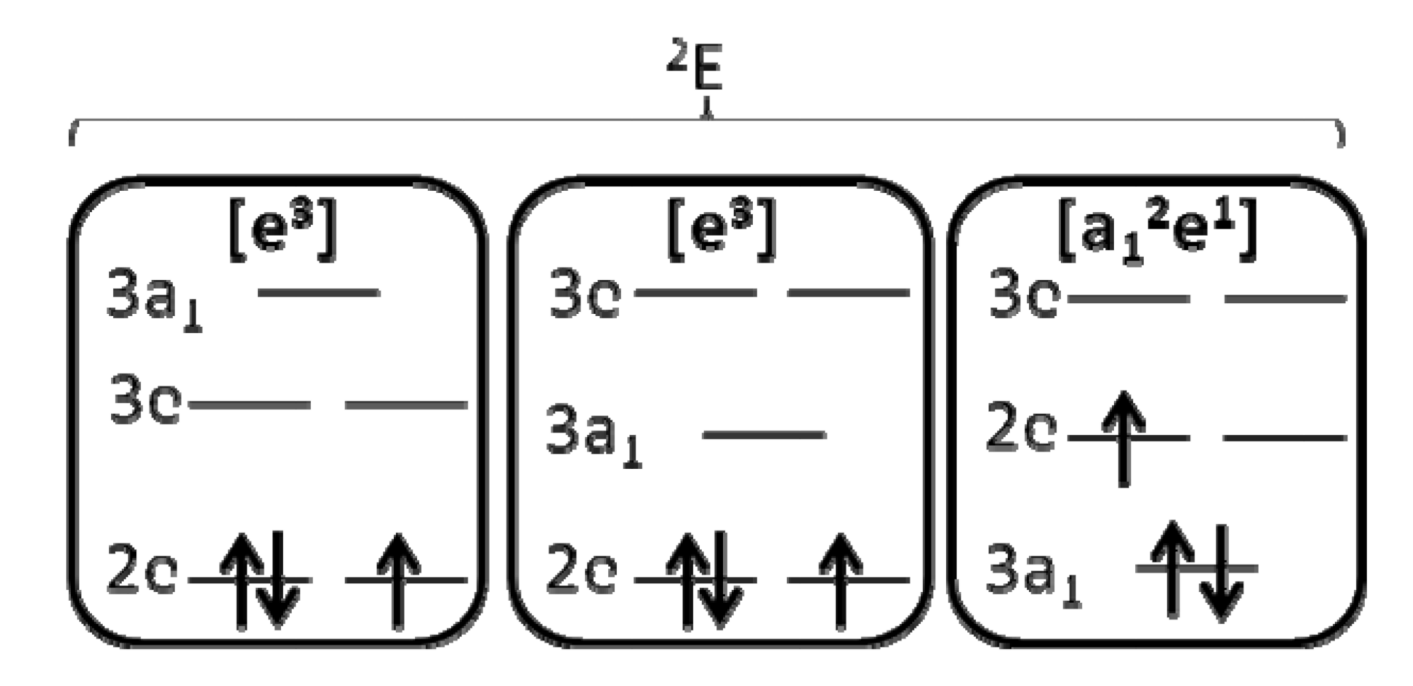


Figure 10.Schematic illustration of the Jahn-Teller active pair of bending modes. Note that the axial ligand is also bending and is hence moving off the symmetry axis.



Scheme 1. Low-spin d^3 frontier orbitals

$$[\textbf{Mo}] N_2 \\ \text{HIPT} \\ \text{Normal Model Normal Model Normal Norm$$

Chart 1.

Table 1

Structural parameters of [Mo]L, L=N₂,CO and NH₃ from X-Ray diffraction and calculations. Model 1':CAS-SCF(3,2)/TZVP/ZORA. Model 1'': BP86/TZVP(Mo,N)/SV(P)(C,H)/ZORA

McNaughton et al.

		\mathbf{Z}_{2}			93			NH_3	
	exp. 1'	1,	1"	exp.*	1,	1,,	exp. 1'		1"
Mo-N _{amido} 1.98 2.01 2.04 (av)	1.98	2.01	2.04		1.99	1.99 2.04 2.00 2.03 2.05	2.00	2.03	2.05
Mo-N _{amine}	2.19	2.19 2.21 2.25	2.25		2.26	2.26 2.29 2.21 2.22	2.21	2.22	2.22
$Mo-N_{\alpha}$	1.96	1.96 2.27 2.01	2.01				2.17	2.17 2.37	2.29
λ_{α} - N_{β}	1.06	1.06 1.07 1.13	1.13						
Mo-C					2.08	2.08 1.98			

All values are given in Å;

 * there are no crystallographic data available for $[\mathbf{Mo}]\mathrm{CO}$

Page 31

Table 2

Calculated excitation energies for d-d transitions (in $\rm cm^{-1}$). Scalar relativistic (ZORA) MR-DDCI2 calculations on top of SA-CASSCF(3,5) reference state (SARC-TZVP basis set).

Term Symbol	Configuration	$[Mo]N_2$	[Mo]CO	[Mo]NH ₃
$^{2}E_{a}$	$(2e)^3$	0	0	0
$^{4}E_{a}$	$(2e)^2(3e)^1$	16979	20644	9188
4A_1	$(2e)^2(3a_1)^1$	30297	32501	18739
$^{2}E_{b}$	$(2e)^2(3e)^1$	23569	26420	21067
$^{2}A_{1}$	$(2e)^2(3a_1)^1$	32947	35454	28692

Transition energies for the first $2e \rightarrow 3e$ and $3e \rightarrow 3a_1$ doublet and quartet transitions

McNaughton et al.

Table 3

Löwdin analysis for the five metal based d-orbitals

		$[Mo]N_2$			[Mo]CO			[Mo]NH3	
	2e	Зе	$3a_1$	2e	Зе	$3a_1$	2e	Зе	$3a_1$
Metal d	79.8%	70.0%	71.8%	70.0% 71.8% 76.3% 68.5% 68.6% 92.5%	68.5%	%9.89	92.5%	74.5%	70.5%
L=N ₂ /CO/NH ₃	15.2%	4.7%	5.7%	18.4%	6.3%	9.2%	1.8%	0.4%	14.7%
$N_{ m amine}$	0.0%	%0.0	6.5%	0.1%	%0.0	2.9%	0.3%	0	6.5%
Equatorial Ligand 3.9% 24.1% 4.9%	3.9%	24.1%	4.9%	4.2%	4.2% 23.8% 4.6%	4.6%	4.3%	4.3% 24.1% 7.5%	7.5%

Page 33

Table 4

Calculated g-values and Pseudo-Jahn-Teller Splittings for different levels of theory (Model 1' geometries, TZVP basis set, ZORA)

McNaughton et al.

		$[Mo]N_2$			[Mo]CO			[Mo]NH ₃		
	CAS(3,2)	CAS(3,5)	MR- DCI2	CAS(3,2)	CAS(3,5)	MR- DCI2	CAS(3,2)	CAS(3,5)	MR- DCI2	
#(roots)	2	30	30	2	30	30	2	30	30	
31	1.14	1.26	1.17	1.80	1.82	1.80	1.43	1.45	1.37	
32	1.14	1.33	1.19	1.80	1.90	1.81	1.43	1.61	1.38	
53	3.50	3.30	2.75	2.77	2.51	2.70	3.23	3.29	3.21	
$\Delta ext{E}_{ ext{PJT}}(ho_0)$	714	735	682	1283	1486	1317	867	862	859	

Page 34

Table 5

Calculated g-values and Pseudo-Jahn-Teller Splittings (Model $\mathbf{1}$ '' geometries, TZVP for Mo and N, SV(P) for C and H)

	$[Mo]N_2$	[Mo]CO	[Mo]NH ₃
g ₁	1.77	1.71	1.36
g_2	1.81	1.76	1.39
g_3	2.66	2.82	3.21
$\Delta E_{PJT}(\rho_0)$ [cm ⁻¹] (Calc/2-orbital)	1309/1200	1096.1200	877/1000